Effects of shield gas flow on meltpool variability and signature in scanned laser melting

David C. Deisenroth[1], Jorge Neira, Jordan Weaver, and Ho Yeung
National Institute of Standards and Technology[2]
Gaithersburg, MD

Author copy Accepted to Proceedings of the ASME 2020 15th International Manufacturing Science and Engineering Conference 2020, June 22-26, 2020, Cincinnati, OH, USA

Abstract

In laser powder bed fusion metal additive manufacturing, insufficient shield gas flow allows accumulation of condensate and ejecta above the build plane and in the beam path. These process byproducts are associated with beam obstruction, attenuation, and thermal lensing, which then lead to lack of fusion and other defects. Furthermore, lack of gas flow can allow excessive amounts of ejecta to redeposit onto the build surface or powder bed, causing further part defects. The current investigation was a preliminary study on how gas flow velocity and direction affect laser delivery to a bare substrate of Nickel Alloy 625 (IN625) in the National Institute of Standards and Technology (NIST) Additive Manufacturing Metrology Testbed (AMMT). Melt tracks were formed under several gas flow speeds, gas flow directions, and energy densities. The tracks were then cross-sectioned and measured. The melt track aspect ratio and aspect ratio coefficient of variation (CV) were reported as a function of gas flow speed and direction. It was found that a mean gas flow velocity of 6.7 m/s from a nozzle 6.35 mm in diameter was sufficient to reduce meltpool aspect ratio CV to less than 15 %. Real-time inline hotspot area and its CV were evaluated as a process monitoring signature for identifying poor laser delivery due to inadequate gas flow. It was found that inline hotspot size could be used to distinguish between conduction mode and transition mode processes, but became diminishingly sensitive as applied laser energy density increased toward keyhole mode. Increased hotspot size CV (associated with inadequate gas flow) was associated with an increased meltpool aspect ratio CV. Finally, it was found that use of the inline hotspot CV showed a bias toward higher CV values when the laser was scanned nominally toward the gas flow, which indicates that this bias must be considered in order to use hotspot area CV as a process monitoring signature. This study concludes that gas flow speed and direction have important ramifications for both laser delivery and process monitoring.

Keywords: metal additive manufacturing, laser powder bed fusion, shield gas flow, plume, condensate, process monitoring

Nomenclature

AR	melt-track aspect ratio
CV	coefficient of variation
HS	hotspot
d	melt-track depth, m
w	melt-track width, m
μ	mean
σ	population standard deviation

1. Introduction

The importance of optimizing shield gas flow is evident from the continuously improving gas flow provisions in industrial laser powder bed fusion machines (LPBF). Inadequate shield gas flow is associated with porosity, lack of fusion defects, decreased strength, increased variability in mechanical properties, and high dimensional inaccuracy in components constructed with LPBF [1–5]. The following sections of this introduction reviews the literature on how laser melting byproducts can affect beam delivery and cause adverse

[1] Contact author: david.deisenroth@nist.gov

effects on laser melting. Process monitoring approaches that may be used to detect adverse effects on melting will then be discussed. Finally, the objective of the current investigation will be described.

1.1 Laser Melting Byproducts

The properties of shield gas play an important role in both laser welding and in LPBF. Types of gas that are used in both laser melting processes include N, Ne, and Ar, and each gas can affect build quality with a given build material [3]. The gas solubility/reactivity with molten metal, and the wettability of the metal in a given gas environment affects keyhole stability and the resulting porosity in laser welding [6]. Finally, gas properties including density, thermal conductivity, and reactivity with metal vapor affect plume generation and persistence [7].

As stated previously, a gas environment that limits reactivity with the metal is insufficient to ensure consistent melting. The need for directional gas flow across the laser-metal interaction stems from the fact that power levels, velocities, and laser focus spot size commonly used for LPBF result in a significant amount of vapor generation at the laser-metal interaction area [8]. This vapor jet, through several mechanisms, produces byproducts that interfere with laser beam delivery. This interference in turn results in insufficient and inconsistent melting of the buildup material, and therefore defects.

The hot vapor jet does not appear to be, in itself, a direct source of beam interference. As the beam passes through the hot vapor, the vapor may become weakly ionized, but inverse Bremsstrahlung absorption due to plasma appears to be small compared to other byproduct effects in metal melting with fiber lasers [9,10]. Beam obstruction due to the metal vapor becomes significant as the vapor condenses in a cloud above the meltpool. When its primary constituent is iron, the metal vapor forms ultrafine condensate particles of 80 nm to 100 nm in diameter with number density of about 10^{10} particles per cm^3 [10]. These clouds of suspended condensate are associated with beam scattering and may attenuate the laser power in excess of 10 % when welding steels with a fiber laser [10]. Furthermore, the hot vapor jet causes localized refractive index changes that may defocus and/or redirect the beam, causing poorly controlled melting [11].

The hot vapor jet also contributes to generation of ejecta that range from 10 μm to 100 μm in diameter via several mechanisms. The high pressure and velocity of the vapor jet and the high surface temperature gradients driving Marangoni flows in the meltpool leads to rapid convection and oscillations that may result in droplet ejection from the meltpool [8]. Beam power oscillations due to condensate obstruction may occur at frequencies up to several kilohertz, which has also been shown to increase liquid ejecta (spatter) in laser welding [10].

In addition to being a driver of meltpool flows, the vapor jet also entrains the ambient gas around it, which may further impel nearby powder particles [12]. The powder can be drawn from the powder-bed from several meltpool widths away from the laser incidence location [8]. The solid metal powder particles, typically of diameter of about 60 μm, may be driven by cold ambient gas convection alone, or they may become entrained directly in the hot vapor jet [8].

Regardless of how they are generated or driven, ejecta of 10 μm to 100 μm in diameter that intersect the beam path may obstruct beam delivery and reduce local melt efficacy. Moreover, this material redistribution from the laser scan path to other areas on the part and powder bed are associated with balling and lack of fusion defects [13]. Finally, material redistribution may interfere with layer recoating, leading to further part defects [14].

Directional gas flow across the laser-metal interaction improves build quality by transporting nanoscale condensate, which reduces beam scattering and attenuation. Directional gas flow also transports microscale ejecta away from the beam path, built part, and powder bed, reducing beam disturbances and defects associated with redistributed material. Finally, directional gas flow also improves the accuracy of beam delivery by reducing thermal lensing by transporting hot gas and vapor from the beam path.

The most practical implementation of directional gas flow is with a single inlet and outlet in the build chamber, as illustrated by the gas flow design of common industrial LPBF machines. This configuration means that the gas flows one direction across the build plane under all conditions. Studies have shown that in LPBF, laser scanning along the direction of the gas flow is associated with increased scanning of airborne ejecta and decreased part tensile strength [14,15]. Scanning along the direction of gas flow is also associated with increased beam interference and particle emissions from suspended condensate in laser welding [9]. Scanning nominally against or perpendicular to the gas flow direction may alleviate these issues [9,14,15]. Similarly, gas flow direction should be considered when developing the hatching directions in scan strategies in order to avoid scanning through suspended condensate or ejecta that were generated by preceding scan tracks—i.e. hatching direction should be nominally toward or perpendicular to gas flow.

1.2 Melt Tracks

In the current investigation, cross-sectioning and measurement of the melt tracks was used as a method to evaluate whether sufficient gas flow was applied to remove byproducts from the beam path. Cross-sectioning and selective etching of solidified melt tracks allow for (destructive) analysis of the meltpool. With this approach, the mode of melting imposed on the substrate, grain structure, and mechanical properties of the solidified material can be evaluated [16,17]. Furthermore, melt track cross-sections are a comparison approach for validating multiphysics modeling results with experimental measurements [18].

The energy density applied to the material has a strong effect on the depth and width of the meltpool, and therefore if significant attenuation or distortion of the beam occurred, that effect was evidenced by the dimensions of the melt tracks. There are varying

definitions of energy density reported in terms of energy per length, energy per volume, etc., but for the purposes of the current discussion, a strict definition of energy density is not necessary. Regardless of definition, it is qualitatively known that the energy density is proportional to applied power and inversely proportional to scan velocity and beam spot size. Therefore, for a given spot size and scan velocity, decreased laser power decreases meltpool width and depth [18]. Beam scattering, attenuation, and lensing may widen the beam, forming a shallower and wider meltpool [11,13].

The energy density applied to the material is also related to the rate of vapor generation from the process. At process conditions producing little to no vapor jet, "conduction mode" occurs. Conduction mode is associated with small meltpool width and depth and an aspect ratio (depth divided by width) of less than unity. Among other defects, too low of energy densities are associated with lack of fusion and balling defects in LPBF [19]. At higher energy densities that result in a high rate of vapor generation, the process transitions into "keyhole mode," in which the meltpool depth increases substantially and the aspect ratio (AR) can become much greater than unity. A steep increase in laser power/energy absorption is associated with the transition from conduction mode to keyhole mode due to the deep cavity formed in the meltpool by the vapor recoil pressure [20–22]. Among other defects, excessive or unstable keyholing is associated with residual porosity and loss of volatile alloy components [6,15]. In the current investigation, meltpool cross-sections will be used to measure the meltpool mode and its variability due to laser delivery with differing gas flow velocities and directions.

1.3 Process Monitoring

Real-time monitoring of the build process to determine part quality is preferred as an alternative to destructive evaluation to assess part quality. Process monitoring approaches have been suggested for assessing homogeneity of the powder bed, surface quality of as built surfaces, and part dimensions during the build [5]. The focus of the current investigation is in assessing the state and consistency of the meltpool in situ as a function of gas flow speed and direction.

A variety of process monitoring approaches relating to meltpool state and consistency have been reported in the literature. Photodetectors mounted on the chamber walls can be used to indicate poor absorption events that are associated with lack of fusion defects [1,23]. High-speed thermal imaging of process spatter and of the hot vapor plume have been investigated as a meltpool monitoring approaches for laser powder bed fusion as well as laser welding [23–25]. The current investigation uses inline imaging of the laser-induced hotspot. The hotspot image processing approach determines the hotspot size and variability. The in-situ hotspot size and variability are then compared with destructively-evaluated meltpool size and variability.

1.4 Objective of the Current Investigation

An example of tracks melted in Nickel Alloy 625 (IN625) with adequate and inadequate gas flow are shown in Figure 1a and Figure 1b, respectively. Both sets of tracks were melted in an argon environment, but one set with adequate gas flow and one with no directional gas flow across the laser-metal interaction area. The tracks with adequate gas flow shown in Figure 1a are highly consistent in width and texture along the length of tracks and from track to track, including the size of the terminal meltpool on the right end of each. In contrast, the tracks with no gas flow shown in Figure 1b are highly inconsistent in width and texture, both along length of tracks and from track to track.

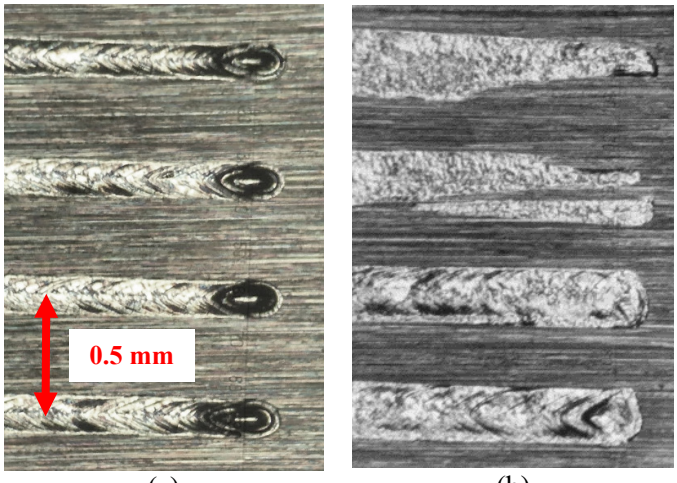

(a) (b)

Figure 1: surface view of tracks laser melted with (a) adequate shield gas flow and (b) no shield gas flow. Both tracks were melted in an argon environment on inconel 625 with a 1070 nm fiber laser, a laser spot D4σ of 100 µm, a scan speed of 400 mm/s, and laser power 150 W. Images are approximately equivalent scale.

And so, it is evident both from the literature and the example shown in Figure 1 that laser melting in an inert gas atmosphere is insufficient, and that a directional gas flow across the laser-metal interaction area is essential to promote consistent melting and ensure final part quality in LPBF. The first goal of the current investigation is to better quantify the meltpool dimensions, AR, and AR variability generated when melting of IN625 in adequate and inadequate gas flow conditions. The second goal of this investigation was to relate melt track cross-sectional AR and AR coefficient of variation (CV) to inline process monitoring hotspot size and hotspot size variability in adequate and inadequate gas flow conditions. The process monitoring effort was undertaken to develop a tool that may identify adverse gas flow effects without destructive evaluation of built parts.

2. Materials and methods

The experiments reported here were performed in the National Institute of Standards and Technology (NIST) Additive Manufacturing Metrology Testbed (AMMT) [26]. The AMMT is a custom LPBF research platform that was designed to be highly configurable for measurement of all aspects of the LPBF process. The AMMT includes a removable carriage that contains the build-well and a large metrology-well, both of which may be moved laterally within the large build chamber. The laser is an Yb-doped fiber laser with emission wavelength of 1070 nm. Laser power delivery can be adjusted from 20 W to more than 400 W, with a 4-sigma diameter (D4σ, representing diameter within which about 95 % of the Gaussian laser power profile is contained) spot size that is adjustable from 45 μm to more than 200 μm. The laser spot can be scanned with full control of the laser scan path/strategy at 100 kHz and laser power control at 50 kHz, with scan velocity from 0 mm/s to more than 4000 mm/s. In the current investigation, the working material was rolled and annealed bare plates of Nickel Alloy 625 (IN625).[3]

2.1 Hotspot Monitoring

The hotspot was imaged with an inline high-speed camera coaxially aligned with the heating laser. Emitted light from the meltpool is filtered by a bandpass filter at 850 nm (40 nm bandwidth at full-width half maximum) and diverted by a dichroic mirror to the camera sensor with nominal 1:1 magnification and 8 μm/pixel size. The images were taken with 45 μs exposure time, 120-pixel x 120-pixel window, and 8-bit grayscale. The grayscale level corresponding to the melting point is roughly determined by comparing the meltpool image with the physical melt-track. This inline meltpool images, therefore, consisted of an approximately circular hotspot with a radiance temperature ranging from approximately 1650 °C to 2050 °C. The camera is triggered by scan position, so the location where each image was taken is known. The equivalent frame rate is 20 kHz.

2.2 Oblique View of Meltpool and Plume

In order to visualize the relationship between the inline meltpool image and the process plume, a second high-speed camera was outfitted with a macroscopic view lens and aligned to obliquely view the meltpool that was scanned perpendicular to the view field. The oblique view camera was outfitted with a spectral filter to the range of approximately 830 nm to 870 nm, which is a similar range to the inline process monitoring camera. The inline and oblique view camera images were synchronized after data was collected.

2.3 Gas Flow Conditions

Gas flow was provided to the process plane at an angle illustrated in Figure 2. Using the coordinate system detailed in Figure 2, the gas flow tube axis was -31° from xz plane and -25° from xy plane. The unit vector formed by the nozzle orientation was $\hat{u} = -0.78\hat{x} - 0.47\hat{y} - 0.42\hat{z}$. The nozzle internal diameter was 6.35 mm. The center of tube outlet was approximately 9 mm in z direction from the surface and approximately 17 mm from the center of the origin shown in Figure 2. The gas flow speed was controlled with a rotameter with average nozzle outlet velocities of 0 m/s, 2.2 m/s, 6.7 m/s, and 22 m/s.

2.4 Scan Strategy

As shown in Figure 2, the IN625 substrate was scanned in six subsequent patches, sequentially as they are numbered. Patches 1 and 2 were scanned with 195 W at 800 mm/s, patch 3 and 4 were scanned with 150 W at 400 mm/s, and patch 5 and 6 were scanned with 195 W at 1200 mm/s. These process parameters are equivalent to those used in the 2018 Additive Manufacturing Benchmark Test Series (AM-Bench) and have very well characterized outcomes [27]. In patches 1, 3, and 5, the scan direction was from top to bottom and tracks were sequentially left to right. In patches 2, 4, and 6, the scan direction was from left to right and tracks were sequentially top to bottom. In other words, odd numbered patches were scanned nominally perpendicular to the gas flow with hatching direction nominally toward the flow and even numbered patches were scanned nominally toward the gas flow with hatching direction nominally perpendicular the flow. This approach facilitated two orthogonal gas flow directions relative to the scan direction. Hatch spacing of 0.5 mm was used to avoid heat accumulation and metallurgical interaction between the tracks. The lowest energy density was applied to

[3] Certain commercial entities, equipment, or materials may be identified in this document to describe an experimental procedure or concept adequately. Such identification is not intended to imply recommendation or endorsement by the National Institute of Standards and Technology, nor is it intended to imply that the entities, materials, or equipment are necessarily the best available for the purpose.

patches 5 and 6, medium energy density was applied to patches 1 and 2, and highest energy density was applied to patches 3 and 4. The D4σ laser spot size used in all experiments was 100 µm.

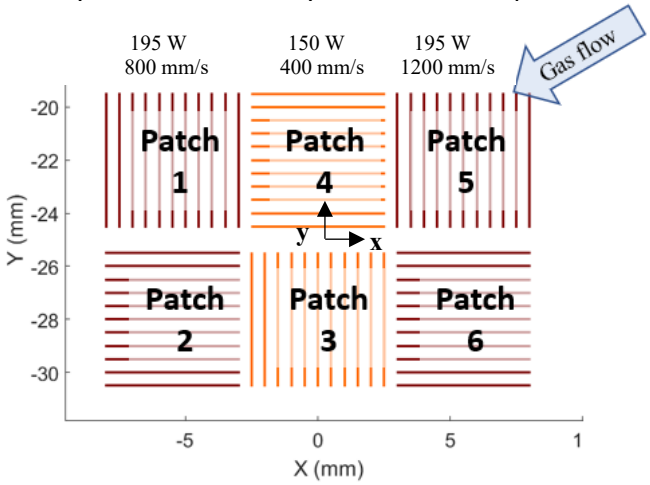

Figure 2: top view of scan tracks applied to the substrate. Coordinates are shown with the origin in the center and the z-axis positive direction out of the image plane.

2.4 Cross-Sectioning

The Ra roughness (defined by ISO 4287:1997, [28]) of the IN625 substrate in which tracks were melted was 19.8 µm with standard deviation between tracks of 3.4 µm. After laser scanning, the substrates were cross-sectioned orthogonal to the scan direction. The sections were 1 mm to 2.5 mm from either end of the melt tracks. Because of the spacing between patches, between 9 and 11 tracks from each patch were sectioned and measured. This sample of tracks from each patch was taken as a random sample of the track cross sections generated by each gas flow speed, scan speed, scan direction, and laser power combination.

Once cut, the substrate samples were hot mounted in mineral filled epoxy thermoset resin, then ground and polished to a mirror-like finish. Next, the mounted samples were etched with aqua regia to enhance contrast between the melt tracks and wrought material. The melt tracks were then optically imaged with 0.155 µm per pixel resolution. An example of a meltpool cross-section image from this work is shown in Figure 3. The meltpool width was measured from the substrate surface intersection with the meltpool edges and the depth was measured from the substrate surface to the deepest point of the meltpool with a pixel-based bounding box.

Figure 3: example image of melt track cross-section image showing locations from which width and depth were measured.

From the width (w) and depth (d) measurements, the aspect ratio (AR) of each meltpool was calculated with Equation (1).

$$AR = \frac{d}{w} \tag{1}$$

Coefficients of variation were calculated for both the meltpool AR and the hotspot area as a measure of how much variability there was from the mean value at each combination of gas flow speed, scan speed, scan direction, and laser power. The coefficient of variation (CV) is simply the standard deviation of the population (σ) divided by the mean (µ) expressed as a percentage, as shown in Equation (2).

$$CV = \frac{\sigma}{\mu} \times 100 \tag{2}$$

2.4 Uncertainty

The laser power of the AMMT was calibrated with a commercial power meter with reported accuracy of 2.5 % and 0.5 % repeatability and is, therefore, assigned 2.6 % uncertainty with 1σ confidence. The spot size has been measured and reported with two

independent methods, and has been shown to be within 10 μm for all measurements taken at 100 μm spot size; Zhirnov et al. [29] compared measurements of the AMMT spot size with both low duty cycle attenuated laser power on a common camera, as well as a dynamic full-power beam sampler. Spot size is therefore assigned a 5 μm uncertainty with 1σ confidence.

The gas flow velocity was set with a manual rotameter that had an uncertainty of approximately 10 %. The orientation of the gas flow nozzle was estimated to be within 10° of the measured value. Gas flow speed and direction accuracy will be improved in future experiments.

Preliminary experiments have found that the uncertainty of change in position on the AMMT laser spot were within 0.25 % and is therefore assigned that value with 1σ confidence. Finally, it was estimated that the subjectivity uncertainty associated with the pixel-based bounding box used to measure meltpool width and depth results in a 67 % likelihood that the meltpool boundary lies within ±5 pixels of the assigned location. Therefore, with a pixel scale 0.155 μm per pixel, the measurement uncertainty is 0.8 μm with 1σ confidence. The uncertainty is summarized in Table 1.

Table 1: uncertainty of measured values with confidence intervals

Measurand	Uncertainty	Confidence
Laser power	2.6 %	1σ
Spot size	5 μm	1σ
Gas flow speed	10 %	Conservative estimate
Gas flow direction (x, y, and z)	5°	Conservative estimate
Track length	0.25 %	1σ
Meltpool width	0.8 μm	1σ
Meltpool depth	0.8 μm	1σ

3. Results and discussion

The experimental results are presented in this section. First, examples of the melt track cross-sections generated under adequate and inadequate gas flow are shown. The AR and AR CV of the tracks as a function of gas flow rate are then presented, then are used as a criteria to define adequate gas flow. Next, the obstructing effect of lack of gas flow on laser delivery is shown with synchronized inline hotspot images and an oblique view of the meltpool and hot vapor plume. After that, the inline hotspot area and its CV are presented as a function of gas flow speed. The relationships between hotspot area, hotspot area CV, meltpool AR, and meltpool AR CV, are finally presented.

3.1 Effects of Gas Flow Speed on Meltpool Cross-Section

This section will first qualitatively, then quantitatively, describe the effects of gas flow speed on meltpool AR and AR CV. Three laser energy densities were applied to the sample, and are shown in increasing order in Figure 4. The lowest energy density was applied in patches 5 and 6, medium energy density was applied in patches 1 and 2, and highest energy density was applied in patches 3 and 4. A gas flow velocity of 6.7 m/s was found to be adequate to remove process byproducts under the conditions tested (to be discussed in more detail further in this section), and is representative of adequate gas flow conditions, as shown in the left column of Figure 4. The right column of Figure 4 shows meltpools generated with no gas flow.

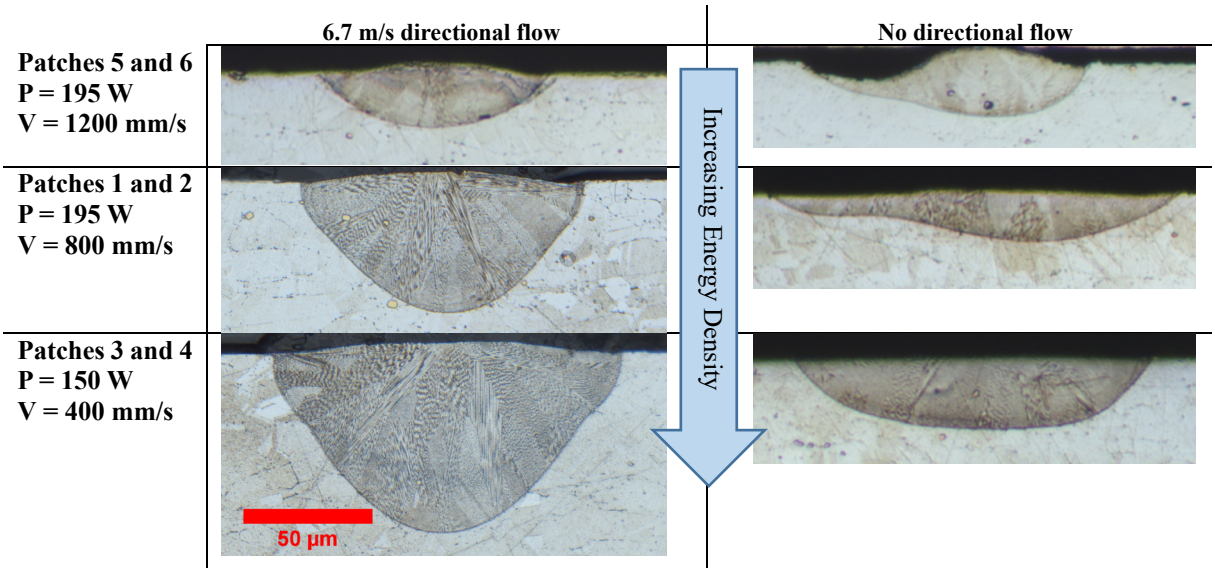

Figure 4: Cross-section views of melt tracks generated with varying energy density and gas flow speed. All tests were with IN625 in an argon environment. All images are same scale.

Starting with the meltpools generated with 6.7 m/s gas flow, the lowest energy density used in patches 5 and 6 forms meltpools in conduction mode with a low AR. With the increased energy density in patches 1 and 2 and 6.7 m/s gas flow, the meltpool width increases slightly and the depth increases significantly, with the AR increasing proportionally. The meltpool mode of patches 1 and 2 is in transition mode. With the

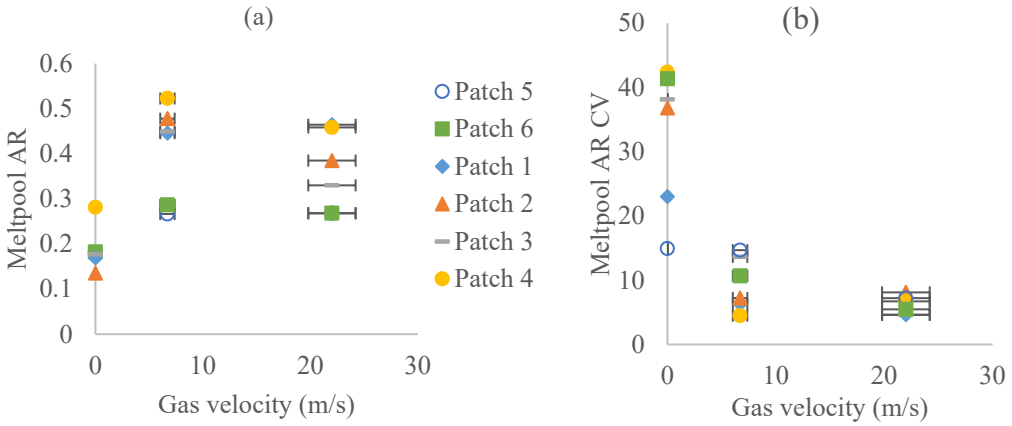

Figure 5: (a) meltpool AR (a) and meltpool AR CV (b) as a function of gas flow speed. Odd numbered patches were scanned nominally perpendicular to the gas flow with hatching direction nominally toward the flow and even numbered patches were scanned nominally toward the gas flow with hatching direction was nominally perpendicular the flow. The lowest energy density was applied to patches 5 and 6, medium energy density was applied to patches 1 and 2, and highest energy density was applied to patches 3 and 4.

highest energy density tested in patches 3 and 4, the meltpool width and depth both increase to the maximum observed. The track generated in patches 5 and 6 are toward keyhole mode than patches 3 and 4, but still in transition mode. All tracks generated with 6.7 m/s gas flow were highly symmetric about their centerline.

The detriment of no directional gas flow is evident in the tests with no directional gas flow, shown in the right column of Figure 4. The melt tracks are consistently asymmetric about their centerline, while also being wider and shallower than those with adequate gas flow. The meltpool depth generally increased with increasing energy density but was highly irregular. These results are consistent with beam scattering, attenuation, and lensing may widen the beam and form a shallower and wider meltpool [11,13].

Figure 5a shows the measured meltpool AR as a function of gas flow speed. With no gas flow, all patches exhibit low AR, generated by shallow and wide meltpools. Because the low energy density tracks (patches 5 and 6) are in conduction mode, they generate little to no vapor, and the low meltpool AR exhibited with no gas flow may be a product of residual suspended condensate from the previous

higher energy density scans. The higher energy density (patches 1 through 4) all exhibit their highest AR at 6.7 m/s. Then, AR decreases slightly for the higher energy density patches from 6.7 m/s to 22 m/s. This decrease in AR is associated with reduced laser delivery and may be a product of excessive gas flow causing rapid condensation directly above the meltpool, which causes slight beam attenuation. This inference is consistent with the very small change observed in the conduction mode patches (patches 5 and 6) from 6.7 m/s to 22 m/s, because there is little or no vapor generated, and therefore, little or no possibility of rapid condensation above the meltpool.

As shown in Figure 5b, increased gas flow rate is associated with decreasing meltpool AR coefficients of variation (CV). With no directional gas flow, patches 4 and 6 exhibited a CV of more than 40, indicating a highly inconsistent process. From 6.7 m/s to 22 m/s, some patches increased slightly in variability and
some decreased slightly, with no clear trend. But, as a whole, the scans with 22 m/s showed less variability than the scans at 6.7 m/s, which appears to be due to the effective (although excessively high velocity) removal of process byproducts from the beam path. Neither the meltpool AR nor AR CV showed a clear dependence on gas flow direction, with both varying stochastically from patch to patch with x-direction scans compared with y-direction scans, as shown in the appendix in Figure 13 and Figure 14.

In summary, the meltpool AR showed only slight changes with a gas flow velocity above 6.7 m/s and the meltpool AR CV fell below 15 % above 6.7 m/s. Therefore, it was a gas flow velocity of 6.7 m/s was said to be “adequate” gas flow to facilitate a consistent process without adverse effects of byproduct accumulation.

3.2 Effects of Gas Flow Speed on Meltpool Signature and Hot Vapor Plume

Figure 6a and b show the synchronized view of the inline meltpool monitoring camera and an oblique view camera at 2,000 fps with adequate gas flow and no gas flow, respectively. As it can be seen that with adequate gas flow (22 m/s), the inline hotspot remains a consistent size and shape from frame to frame. Similarly, with adequate gas flow, the hotspot in the oblique view remains a consistent size and shape. The hot vapor jet can be seen directly above the oblique view hot spot, and although the jet size, shape, and direction vary slightly, its general profile remains quite consistent throughout the sequence.

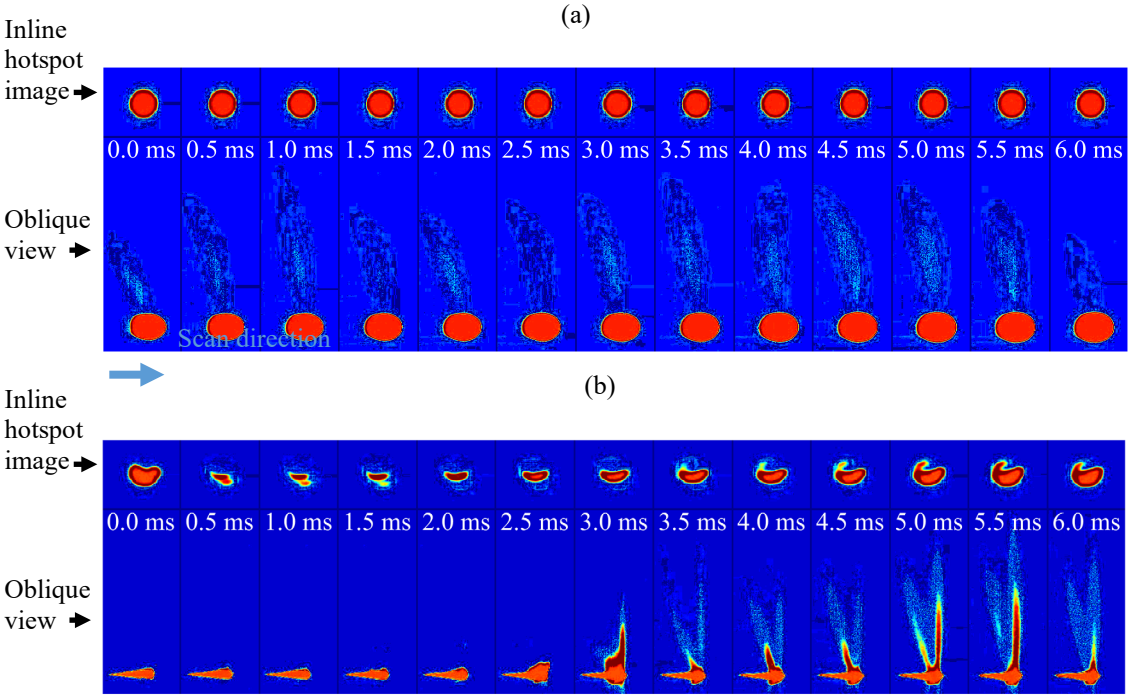

Figure 6: inline hotspot image synchronized with an oblique view of meltpool and vapor plume with (a) 22 m/s directional gas flow and (b) no directional gas flow. Both tracks were melted in an argon environment on IN625 with a 1070 nm fiber laser, a laser spot D4σ of 100 µm, a scan speed of 400 mm/s, and laser power 150 W. The inline and oblique view images were taken at nominally 850 nm wavelength. Images are gamma-adjusted to enhance contrast, so intensity is not directly indicative of temperature.

In contrast with adequate gas flow, it can be seen in Figure 6b that the inline hotspot image is changing significantly in size and shape along the length of the track. The hotspot in the oblique view changes in size and shape slightly, but the vapor jet changes significantly along the length of the track. From 0.0 ms to 2.5 ms, no vapor jet is visible, suggesting that the beam energy density is diminished so much that vapor generation is not occurring during that period, indicating that the beam is scattered and attenuated by lingering condensate generated by previous tracks. After 2.5 ms, the vapor jet re-forms with rapidly changing size and shape until its

endpoint at 6.0 ms. This obstruction of beam delivery is consistent with the findings of Shcheglov et al. [10] when gas flow inadequately removed process byproducts from the beam path in laser welding. In comparing Figure 6a and b, it is evident that a large and consistent inline hotspot size is associated with a consistent vapor jet from the meltpool.

Figure 7a shows an optical image of a set of melt tracks (all 6 patches) generated with 22 m/s directional gas flow. In Figure 7a, the tracks are visibly consistent in width and texture along the length of each track and repeatable from track to track. The chevron patterns are relatively evenly spaced and the terminal meltpool at the end of each track have consistent sizes for each set of process parameters. Figure 7b shows a contour plot of the inline image pixel count (above 80 digital levels) at each location along scan path of the track shown in Figure 7a. The number of pixels is proportional to the area of the laser-metal interaction. The hotspot area is largest in patches 1 through 4, at about 600 pixels to more than 800 pixels. The large hotspot area is generated by the higher laser energy density applied in those patches. The smallest hot spot is generated in patches 5 and 6, in the range of about 400 pixels because of the lower energy density applied to

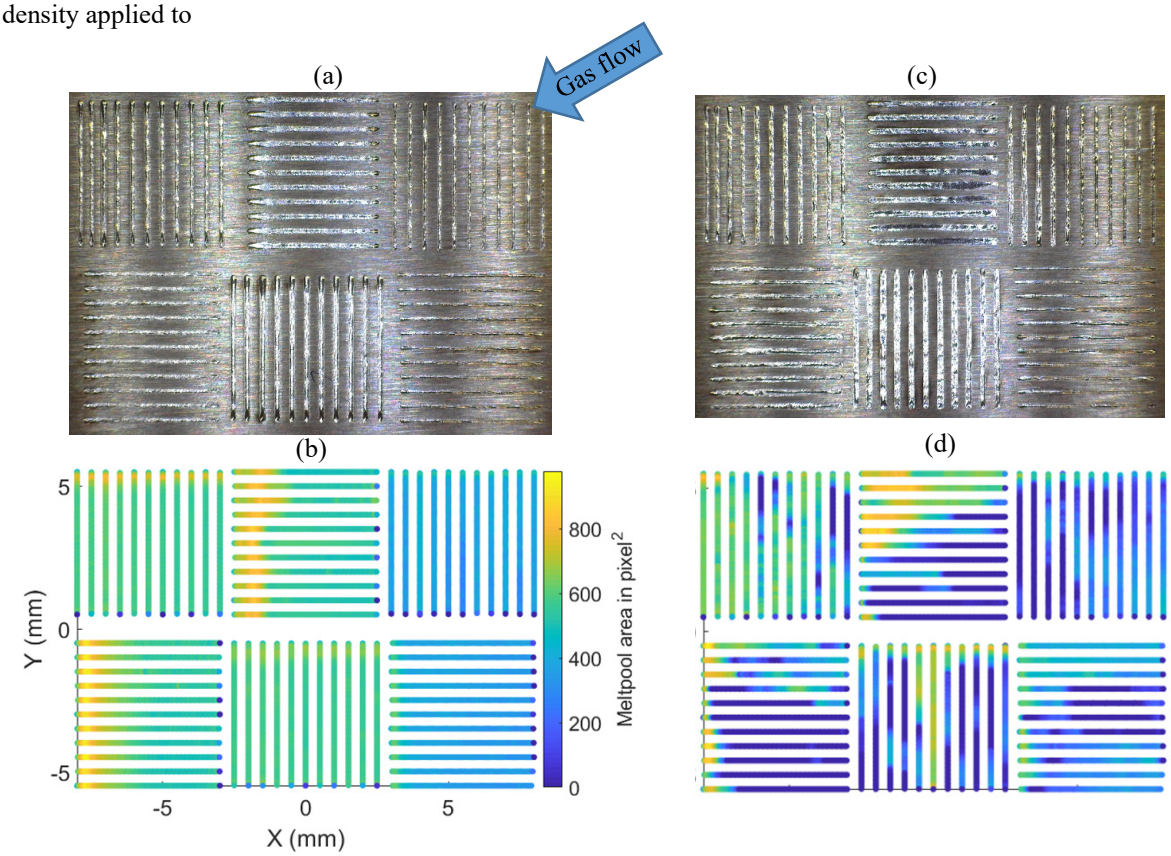

Figure 1: (a) surface image of tracks melted with 22 m/s directional gas flow, (b) contour plot of inline image hotspot pixel count at each location along tracks of (a), (c) surface image of tracks melted with no directional gas flow, (d) contour plot of inline image hotspot pixel count at each location along tracks of (c)

those patches. The hotspot size is quite consistent and repeatable along the length of each line and from line to line.

In contrast to Figure 7a, Figure 7c shows that the melt tracks are visibly inconsistent with no directional gas flow applied to the process. The melt tracks are unstable, unrepeatable, and highly variable in width and texture. The hotspot contour map in Figure 7d shows high variability in the hotspot size, ranging from nearly 0 to 800 pixels sporadically along the length of the tracks and from track to track. Areas of small hotspot size appear to correlate with visible widenings in the melt tracks. The only track with low variability is the first track scanned (furthest left in patch 1) because of the lack of accumulated suspended condensate in the beam path.

Figure 8a shows the relationship between hotspot area and gas flow speed. From 0 m/s to 6.7 m/s all patches show an increasing trend in hotspot area with gas flow speed, with slightly more scatter occurring at 2.2 m/s compared with 0 m/s. From 6.7 m/s to 22 m/s, each patch hotspot size decreases slightly. This is likely due to rapid condensation of vapor directly above the meltpool caused by the excess gas flow, as was discussed previously. This condensate directly above the meltpool may attenuate the beam and reduce the beam energy density delivered to the process. The condensate directly above the meltpool may also attenuate the light emitted from the process and detected by the inline imager. No clear trend was associated with hot spot size and scan direction relative to the gas flow direction, as is shown in Appendix Figure 12.

Figure 8b shows that from 0 m/s to 6.7 m/s all patches show a monotonic decrease in hotspot CV, with the exception of patch 5 at 2.2 m/s. After 6.7 m/s, all patches show a slight increase in the hotspot variability. The slight increase in hotspot variability at 22 m/s may be due to increased emission and emission variability from the rapidly condensing
vapor jet directly above the meltpool, essentially generating a "flickering" effect and an apparent increase in hotspot variability interpreted by the inline imager. The trend observed in hot spot
size variability with meltpool AR variability as a function of scan direction will be discussed in the following section.

3.3 Relationship Between Hotspot Area and Meltpool Aspect Ratio

One of the intentions of the current investigation was to better understand the relationship between inline image hotspot size and meltpool AR, and the results are shown in Figure 9. With no gas flow, there is a significant amount of scatter in the average hotspot size produced in each patch; the hotspot size is also generally smaller with no gas flow than with ≥6.7 m/s in each patch. With gas flow ≥6.7 m/s there is an increasing trend with hotspot area and meltpool AR in each path. In the low energy density patches in conduction mode (patches 5 and 6), that generate an AR of about 0.3, a hotspot size of about 0.25 mm^2 was generated. In the higher energy density patches (patches 1 through 4) with AR greater than 0.3, the hotspot size increased to about 0.04 mm^2. It can be observed that in transition mode (AR > 0.3), HS area increases only slightly with a significant increase in meltpool AR. This lack of sensitivity of hotspot area to meltpool AR indicates that hotspot area is a diminishingly

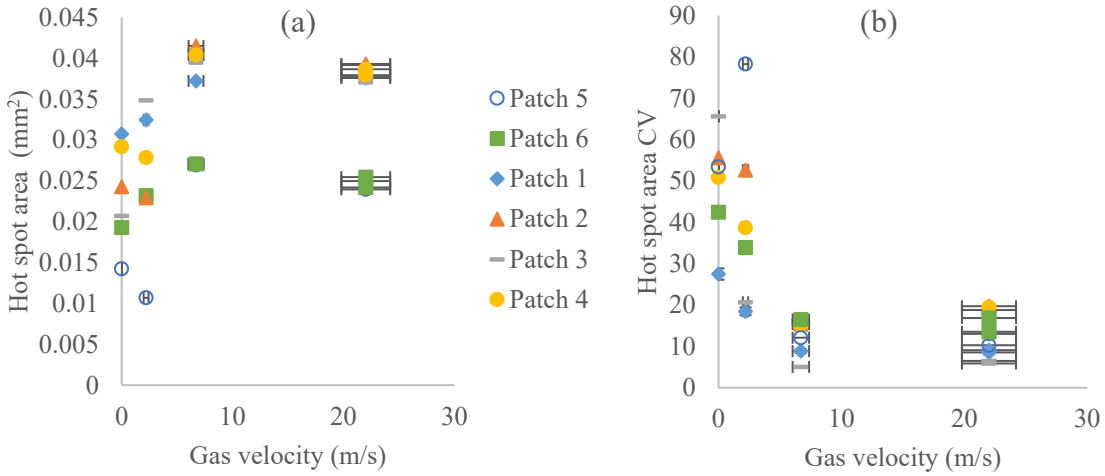

Figure 8: (a) hotspot area and (b) hotspot area cv as function of directional shield gas flow rate

useful indicator as the process transitions toward keyhole mode. Under the conditions tested, the HS area could be used to discern between conduction mode and transition mode processes, but may not be a useful process signature for processes with higher energy densities than early transition mode.

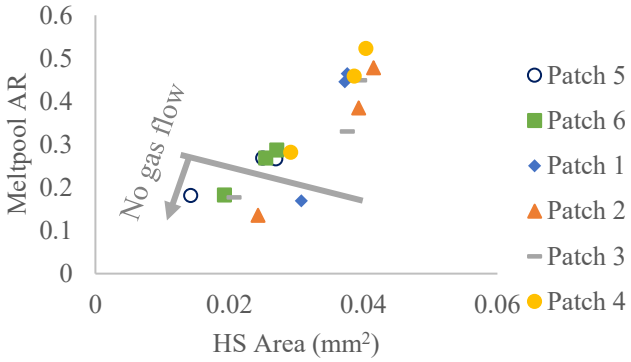

Figure 9: hotspot area as a function of meltpool AR

Hotspot area CV as a function of meltpool AR coefficient of variability was found to be a stronger indicator of the extreme process variability associated with inadequate gas flow than average hotspot size was, as shown in Figure 10. Meltpool AR coefficients of variation greater than 14.8 were associated with no gas flow. With no gas flow, the hotspot area CV increased by a factor of about two

when compared to the hot spot CV generated with adequate gas flow of ≥6.7 m/s, producing a clear indication of meltpool AR variability. It can be seen, though, that with gas flow ≥6.7 m/s, the hotspot area coefficient of variability splits into two distinct groups: x-scan direction and y-scan direction. With gas flow ≥6.7 m/s and comparable meltpool AR coefficients of variation, the hotspot area coefficients of variation show a significant bias toward higher values when scanning in the x-direction, which is toward the gas flow. With scan direction relative to gas flow direction being the only variable changed, it is likely that a plume effect is the cause of the increased "flicker" in the inline hotspot size.

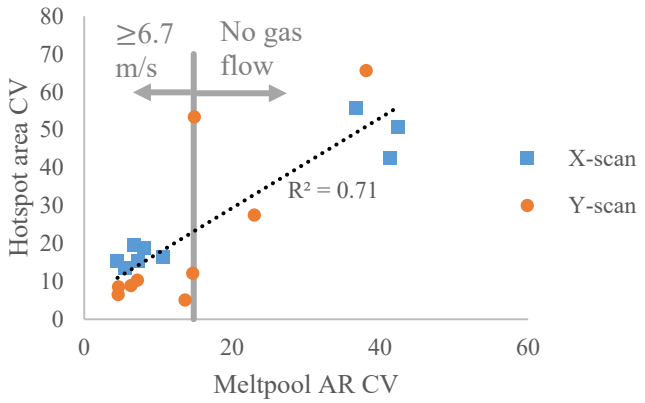

Figure 10: hotspot area cv as a function of meltpool ar variability. X-scans are nominally toward the gas flow, y-scans are nominally perpendicular to the gas flow

The inline hotspot area CV generated with patches scanned in the x-direction compared with the y-direction are shown in Figure 11. As would be expected, there is a significant amount of scatter with no discernable pattern in the region with no gas flow, which exhibits coefficients of variation greater than 30. But, a quite clear trend emerges in the region with gas flow ≥6.7 m/s, in which the amount of bias toward higher hotspot variability increases with increasing process energy density.

With patches 5 and 6 in conduction mode, little or no vapor is generated, and the bias toward higher variability in the x-direction is small with gas flow ≥6.7 m/s. The bias increases with higher process energy density. At the highest process energy density, scans in the x-direction exhibit 3 to 4 times higher hotspot coefficients of variation with gas flow ≥6.7 m/s. This increasing variability in hotspot size, therefore, appears to be a function of laser interaction with the hot vapor jet differently when scanning nominally toward the gas flow compared with nominally perpendicular to the gas flow. It seems particularly likely that the increased variability in hotspot size with scan direction is due to the hot vapor jet considering that no clear scan-direction bias was found in meltpool AR, meltpool AR CV, or hotspot area. The cause of hotspot area CV changes with scan direction are currently unknown but may be related to increased vapor jet velocity relative to the gas flow and/or changes in vapor jet incline angle with gas flow direction.

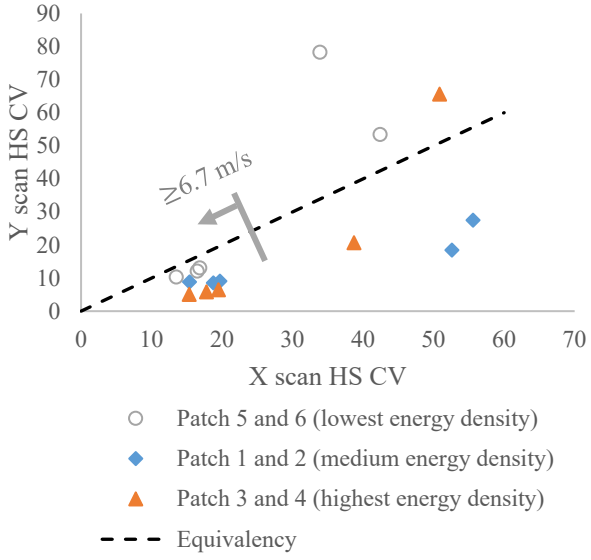

Figure 11: inline hotspot CV at three power densities with x and y scan directions

4. Conclusion

A preliminary study on the effects of gas flow speed and direction on meltpool aspect ratio and hotspot size was performed under process parameters similar to those used in LPBF in IN625. It was found that no gas flow was associated with asymmetric, shallow, and wide melt tracks that may cause lack of fusion defects. The melt tracks became consistent in width, depth, and shape with adequate gas flow. Excessive gas flow was associated with higher consistency in meltpool aspect ratio, but shallower meltpools.

For process monitoring, it was found that, under the conditions tested, inline image hotspot size increased with energy densities that formed meltpools ranging from conduction mode to transition mode. Average hotspot area was, though, a relatively insensitive indicator of both meltpool aspect ratio and high process variability, especially as the energy density increased in the transition mode toward keyhole mode. Hotspot area coefficient of variation was found to be a stronger indicator of meltpool aspect ratio variability, and therefore an indicator of inadequate gas flow. Use of hotspot area coefficient of variation as an indicator of meltpool aspect ratio variability suffered from a bias toward higher variability when the meltpool was scanned nominally toward the gas flow. The bias that caused higher "flicker" in the meltpool image hotspot area was likely due to a change in the laser interaction with the hot vapor jet with different gas flow directions. Therefore, it is concluded that gas flow speed and direction each have important ramifications for both laser delivery and process monitoring.

Future work will be in developing gas flow profiles (especially increased height of the velocity profile) that are compatible with LPBF powders, as the velocities used in this study would likely disrupt the powder bed. This study has improved the understanding of the relationship between meltpools and meltpool signature, but more work is needed to develop robust process monitoring. Meltpool image intensity and intensity variability will be investigated in future work.

ACKNOWLEDGEMENTS

The authors wish to thank Brandon Lane of the NIST Engineering Laboratory for his help with uncertainty estimates and Sergey Mekhontsev of the NIST Physical Measurement Laboratory for his aid in setup of the plume visualization experiments.

REFERENCES

[1] Coeck, S., Bisht, M., Plas, J., and Verbist, F., 2019, "Prediction of Lack of Fusion Porosity in Selective Laser Melting Based on Melt Pool Monitoring Data," Additive Manufacturing, 25, pp. 347–356.

[2] Ferrar, B., Mullen, L., Jones, E., Stamp, R., and Sutcliffe, C. J., 2012, "Gas Flow Effects on Selective Laser Melting (SLM) Manufacturing Performance," Journal of Materials Processing Technology, 212(2), pp. 355–364.

[3] Bean, G. E., Witkin, D. B., McLouth, T. D., and Zaldivar, R. J., 2018, "The Effect of Laser Focus and Process Parameters on Microstructure and Mechanical Properties of SLM Inconel 718," Laser 3D Manufacturing V, International Society for Optics and Photonics, p. 105230Y.

[4] Kong, C.-J., Tuck, C. J., Ashcroft, I. A., Wildman, R. D., and Hague, R., 2011, "High Density Ti6Al4V via SLM Processing: Microstructure and Mechanical Properties," International Solid Freeform Fabrication Symposium, pp. 475–483.

[5] Malekipour, E., and El-Mounayri, H., 2018, "Common Defects and Contributing Parameters in Powder Bed Fusion AM Process and Their Classification for Online Monitoring and Control: A Review," Int. J. Advanced Manufacturing Technology, 95(1–4), pp. 527–550.

[6] Elmer, J. W., Vaja, J., Carlton, H. D., and Pong, R., 2015, "The Effect of Ar and N2 Shielding Gas on Laser Weld Porosity in Steel, Stainless Steels, and Nickel," Weld J., 94(10), pp. 313s–325s.

[7] Ahn, J., He, E., Chen, L., Dear, J., and Davies, C., 2017, "The Effect of Ar and He Shielding Gas on Fibre Laser Weld Shape and Microstructure in AA 2024-T3," J. Manufacturing Processes, 29, pp. 62–73.

[8] Ly, S., Rubenchik, A. M., Khairallah, S. A., Guss, G., and Matthews, M. J., 2017, "Metal Vapor Micro-Jet Controls Material Redistribution in Laser Powder Bed Fusion Additive Manufacturing," Scientific Reports, 7(1), p. 4085.

[9] Shcheglov, P., 2012, "Study of Vapour-Plasma Plume during High Power Fiber Laser Beam Influence on Metals," Ph.D. thesis, BAM Federal Institute for Materials Research and Testing.

[10] Shcheglov, P. Y., Gumenyuk, A. V., Gornushkin, I. B., Rethmeier, M., and Petrovskiy, V. N., 2012, "Vapor–Plasma Plume Investigation during High-Power Fiber Laser Welding," Laser Physics, 23(1), p. 016001.

[11] Katayama, S., Kawahito, Y., and Mizutani, M., 2010, "Elucidation of Laser Welding Phenomena and Factors Affecting Weld Penetration and Welding Defects," Physics Procedia, 5, pp. 9–17.

[12] Zhirnov, I., Kotoban, D. V., and Gusarov, A. V., 2018, "Evaporation-Induced Gas-Phase Flows at Selective Laser Melting," Applied Physics A, 124(2), p. 157.

[13] Ladewig, A., Schlick, G., Fisser, M., Schulze, V., and Glatzel, U., 2016, "Influence of the Shielding Gas Flow on the Removal of Process By-Products in the Selective Laser Melting Process," Additive Manufacturing, 10, pp. 1–9.

[14] Anwar, A. B., and Pham, Q., 2016, "Effect of Inert Gas Flow Velocity and Unidirectional Scanning on the Formation and Accumulation of Spattered Powder during Selective Laser Melting," 2nd Intl. Conf. on Progress in Additive Manufacturing, Singapore, pp. 531 – 536.
[15] Aboulkhair, N. T., Everitt, N. M., Ashcroft, I., and Tuck, C., 2014, "Reducing Porosity in AlSi10Mg Parts Processed by Selective Laser Melting," Additive Manufacturing, 1, pp. 77–86.
[16] Weaver, J. S., Kreitman, M., Heigel, J. C., and Donmez, M. A., 2019, "Mechanical Property Characterization of Single Scan Laser Tracks of Nickel Superalloy 625 by Nanoindentation," TMS 2019 148th Annual Meeting & Exhibition Supplemental Proceedings, Springer, pp. 269–278.
[17] Keller, T., Lindwall, G., Ghosh, S., Ma, L., Lane, B. M., Zhang, F., Kattner, U. R., Lass, E. A., Heigel, J. C., and Idell, Y., 2017, "Application of Finite Element, Phase-Field, and CALPHAD-Based Methods to Additive Manufacturing of Ni-Based Superalloys," Acta Materialia, 139, pp. 244–253.
[18] Ghosh, S., Ma, L., Levine, L. E., Ricker, R. E., Stoudt, M. R., Heigel, J. C., and Guyer, J. E., 2018, "Single-Track Melt-Pool Measurements and Microstructures in Inconel 625," JOM, 70(6), pp. 1011–1016.
[19] Yadroitsau, I., 2009, Selective Laser Melting: Direct Manufacturing of 3D-Objects by Selective Laser Melting of Metal Powders, Lambert Academic Publishing.
[20] Trapp, J., Rubenchik, A. M., Guss, G., and Matthews, M. J., 2017, "In Situ Absorptivity Measurements of Metallic Powders during Laser Powder-Bed Fusion Additive Manufacturing," Applied Materials Today, 9, pp. 341–349.
[21] Ye, J., Khairallah, S. A., Rubenchik, A. M., Crumb, M. F., Guss, G., Belak, J., and Matthews, M. J., 2019, "Energy Coupling Mechanisms and Scaling Behavior Associated with Laser Powder Bed Fusion Additive Manufacturing," Advanced Engineering Materials, p. 1900185.
[22] Simonds, B. J., Sowards, J., Hadler, J., Pfeif, E., Wilthan, B., Tanner, J., Harris, C., Williams, P., and Lehman, J., 2018, "Time-Resolved Absorptance and Melt Pool Dynamics during Intense Laser Irradiation of a Metal," Phys. Rev. Applied, 10(4), p. 044061.
[23] Spears, T. G., and Gold, S. A., 2016, "In-Process Sensing in Selective Laser Melting (SLM) Additive Manufacturing," Integrating Materials and Manufacturing Innovation, 5(1), pp. 16–40.
[24] Ye, D., Zhu, K., Fuh, J. Y. H., Zhang, Y., and Soon, H. G., 2019, "The Investigation of Plume and Spatter Signatures on Melted States in Selective Laser Melting," Optics & Laser Technology, 111, pp. 395–406.
[25] Tenner, F., Brock, C., Klämpfl, F., and Schmidt, M., 2015, "Analysis of the Correlation between Plasma Plume and Keyhole Behavior in Laser Metal Welding for the Modeling of the Keyhole Geometry," Optics and Lasers in Engineering, 64, pp. 32–41.
[26] Lane, B., Mekhontsev, S., Grantham, S., Vlasea, M., Whiting, J., Yeung, H., Fox, J., Zarobila, C., Neira, J., and McGlauflin, M., 2016, "Design, Developments, and Results from the NIST Additive Manufacturing Metrology Testbed (AMMT)," Solid Freeform Fabrication Symposium, Austin, TX, pp. 1145–1160.
[27] Levine, L., Lane, B., Heigel, J., Migler, K., Stoudt, M., Phan, T., Ricker, R., Strantza, M., Hill, M., Zhang, F., Seppala, J., Garboczi, E., Bain, E., Cole, D., Allen, A., Fox, J., and Campbell, C., 2020, "Outcomes and Conclusions from the 2018 AM-Bench Measurements, Challenge Problems, Modeling Submissions, and Conference," Integrating Materials and Manufacturing Innovation.
[28] ISO, 1997, "Geometrical Product Specifications (GPS)–Surface Texture: Profile Method–Terms, Definitions and Surface Texture Parameters," 4287.
[29] Zhirnov, I., 2019, "Dynamic Measurement of Laser Beam Quality for Selective Laser Melting," Presented at Solid Freeform Fabrication Symposium, Austin.

Appendix

As shown in Figure 12, there is no clear gas flow direction bias in hotspot area. As shown in Figure 13, no trend was observed due to scan direction in meltpool AR. As shown in Figure 14, no clear bias is shown in meltpool AR CV due to scan direction.

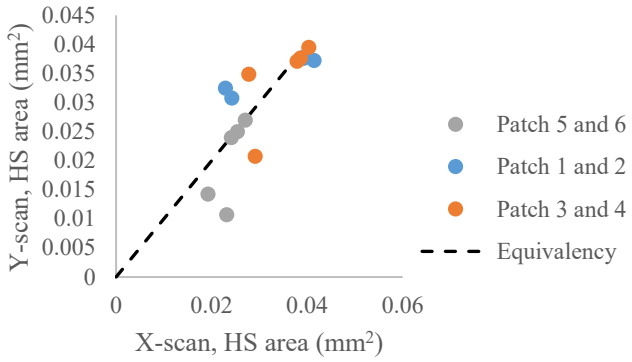

Figure 12: hot spot size bias with scan direction

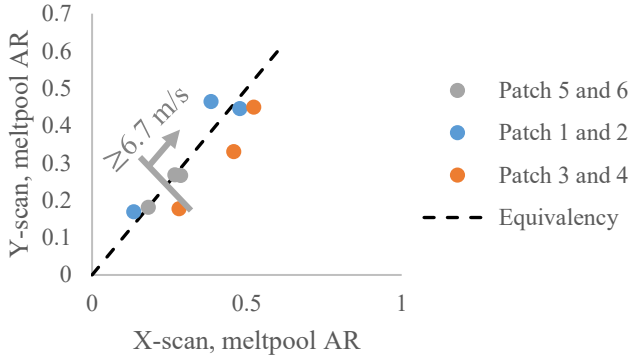

Figure 13: meltpool aspect ratio direction dependence

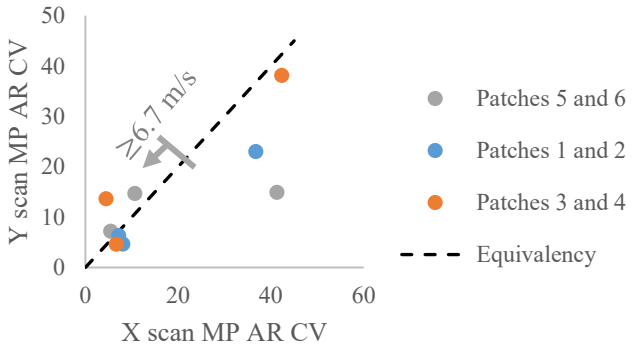

Figure 14: meltpool aspect ratio cv direction dependence